Electronic Supplementary Information

Turn-On Ratiometric Ag^+ Sensing Aids In Situ Synthesis of NIR Emissive Silver Nanoclusters

Palani Yuvaraj[a], Jayaraman Narayanan[a], Joseph Ajantha[a,b], Masiyappan Karuppusamy,[c] Muthuramalingam Prakash,[c,d] Jonalagadda Raghava Rao[a] and Shanmugam Easwaramoorthi[a]*

[a]Inorganic & Physical Chemistry Laboratory, CSIR-Central Leather Research Institute, Chennai – 600 020, India.

[b]Centre for Analysis, Testing, and Reporting Services (CATERS), CSIR-Central Leather Research Institute, Chennai – 600 020, India.

[c]Computational Chemistry Research Laboratory (CCRL), Department of Chemistry, SRM Institute of Science and Technology, Kattankulathur – 603 203, India.

[d]Centre for Advanced Computational and Theoretical Sciences (ACTS), SRM Institute of Science and Technology, Kattankulathur – 603 203, India.

* Corresponding author: moorthi.clri@csir.res.in

TABLE OF CONTENTS

1. Discussion

Molecular rotor behavior of the probes

The weakly fluorescent nature of both EC-BA, and EC-TBA originated from the molecular rotor is explained as follows. Upon photoinduced ICT, in the CT state of the chromophore the double bond connecting the carbazole and BA/TBA adopts a single bond character, thereby enabling the free rotation of the acceptor with respect to the donor. This conformational flexibility at the excited states accelerates the non-radiative decay channel, rendering these molecules weakly fluorescent, The rotor behavior of the probe was further understood from the viscosity dependent fluorescence measurements. Increasing the solution viscosity by dissolving polystyrene in THF resulted in a significantly enhanced fluorescence as depicted in Fig. S8. Higher viscosity restricts the intramolecular rotation after ICT thereby supresses the nonradiative decay channels leading to enhanced fluorescence. To further elucidate the origin of weak fluorescence, we examined the torsional dependence of the electronic structure using a relaxed S_0 potential energy scans and rigid S_1 TD-DFT single-point calculations. The C1-C28-C29-C30 dihedral angle, which defines the primary donor-acceptor rotational axis was chosen for analysis (Fig. S9). The relaxed S_0 torsional PES shows a substantial ~48 kcal mol^{-1} barrier between planar and orthogonal conformations, indicating a strongly conjugated D–A π-framework and limited rotation about the C28–C29 bond, consistent with its short, partial double-bond character (~1.367 Å). The rigid S_1 scan reveal pronounced angular modulation of the optical response, the S_1 oscillator strength collapses near 90° and 270°, where donor and acceptor become orthogonal and π-conjugation is disrupted. These geometries produce a dark ICT state with low transition probability, suggesting that donor–acceptor twisting is responsible for EC-TBA's weak fluorescence.

pH- Dependent studies

pH-dependent fluorescence studies show that Ag-nanocluster emission is strongest at neutral pH, while both acidic and basic conditions cause significant quenching (Fig S17). Our results show that the fluorescence intensity is highest at neutral pH, whereas both acidic and basic conditions lead to significantly reduced emission. This behavior indicates that the formation and stabilization of the Ag nanoclusters are highly sensitive to pH. Under acidic conditions, protonation of the ligand framework likely disrupts Ag^+ coordination, while in basic media, competing hydroxide coordination may hinder nanocluster formation.

The optimal fluorescence response at neutral pH confirms that stable Ag nanocluster formation is influenced by the pH and thus effective sensing occurs most efficiently under near-neutral conditions.

MALDI TOF Mass Analysis

To estimate the number of silver atoms present in the nanocluster, we carried out MALDI-TOF-MS analysis of the sample in methanol. The prominent peaks at m/z 919, 1071, and 1185 (Fig. S15) was observed. Based on the characteristic ligand-fragmentation behaviour typically observed under MALDI ionization and by correlating these masses with reported silver nanocluster series, the detected signals most plausibly correspond to a silver cluster comprising of approximately Ag_9–Ag_{11} atoms.

2. EXPERIMENTAL SECTION

All reagents and chemicals were purchased from commercial sources (Aldrich, Across, Fluka) and used without further purification unless stated otherwise. All solvents were distilled over appropriate drying agent(s) prior to use and were purged with nitrogen. Column chromatography purification was performed by using silica gel (100-200 mesh) as a stationary phase and chloroform or *n*-hexane and ethyl acetate mobile phase. ^{1}H NMR spectra were recorded on Bruker spectrometer (400 MHz) and are reported in *ppm* (parts per million) units relative to the signals for residual chloroform (7.26 *ppm*) and DMSO (2.54 *ppm*) in the deuterated solvent. ^{13}C NMR spectra were recorded on Bruker spectrometer (100 MHz) and are reported in *ppm* relative to deuterated chloroform (77.23 *ppm*), DMSO (39.52 *ppm*) with dropwise (TMS) as an internal standard. Coupling constants (*J*) are reported in Hz; splitting patterns are assigned *s* = singlet, *d* = doublet, *t* = triplet, *q* = quartet, *br* = broad signal. UV-Visible absorption spectra were measured using a Shimadzu UV-1800 spectrophotometer. The steady-state and time-resolved fluorescence were measured using Edinburg, FLS980 spectrofluorometer. Dynamic light scattering (DLS) was performed on a Zetasizer Nano ZS using 4 mW He/Ne laser (632.8 nm wavelength) with a scattering angle of 175°. The obtained particle size was an average of five separate measurements, and the measurement uncertainty was indicated as the standard deviation. A quartz cuvette with inverse centimetre optical path length was used. X-ray photoelectron spectroscopy (XPS) was performed on an Omicron Nano Technology (UK) spectrometer equipped with an Al Kα X-ray source. Transmission electron microscopy (TEM) images and selected area electron diffraction (SAED) patterns were obtained using JEOL JEM-2100 Plus and Talos F200X G2 transmission electron microscopes.

All electronic structure calculations were performed using Gaussian 16 (Revision A.03).[1] The ground state geometry optimization of the neutral EC-TBA system was carried out at the CAM-B3LYP level of theory with Grimme's D3 empirical dispersion correction.[2-3] The 6-31G(d,p) basis set was used for all main-group atoms (C, H, N, O and S).[4] The optimized geometries were confirmed as minima by the absence of imaginary vibrational frequencies. Relaxed ground-state (S_0) torsional scans were performed by constraining the 1-28-29-30 dihedral angle from 0° to 360° in 10° increments. For each constrained angle, the geometry was optimized using Opt=(ModRedundant). Rigid excited-state scans were performed using single-point TD-DFT calculations at the S_1 state (NStates=1) on each relaxed S_0 geometry. All calculations were performed without symmetry constraints (Nosymm).

2.1. Synthesis of 5-((9-ethyl-9H-carbazol-3-yl)methylene)pyrimidine-2,4,6(1H,3H,5H)-trione (EC-BA)

Scheme S1

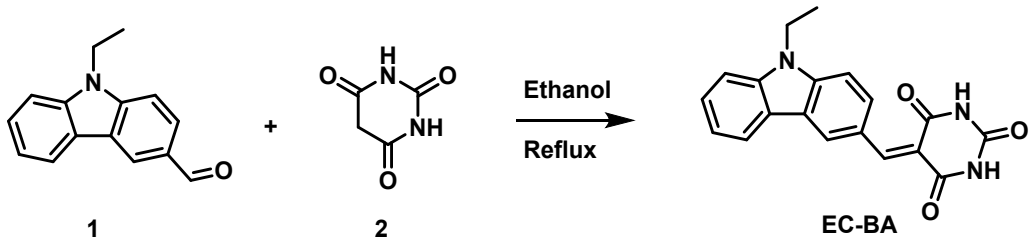

In a 100 mL round bottom flask, 9-ethyl-9H-carbazole-3-carbaldehyde (1) (0.5 g and 2.2 mmole) and barbituric acid (2) (0.2817 g and 2.2 mmol) were dissolved in 30 mL of ethanol. The mixture was refluxed overnight with stirring at 85 °C during which a yellow precipitate was formed. The precipitate was separated by filtration using Whatman filter paper 42 and washed thrice with 20 mL of cold ethanol and the product was then dried using rotary evaporator which offered yellow solid (0.48 g yield 85 %) .1H NMR (400 MHz, DMSO-d6) δ 11.31 (s, 1H), 11.19 (s, 1H), 9.27 (s, 1H), 8.61 (dd, J = 8.9, 1.7 Hz, 1H), 8.52 (s, 1H), 8.17 (d, J = 7.7 Hz, 1H), 7.68 (t, J = 8.3 Hz, 2H), 7.52 (ddd, J = 8.3, 7.1, 1.2 Hz, 1H), 7.35 – 7.26 (m, 1H), 4.47 (q, J = 7.1 Hz, 2H), 1.33 (t, J = 7.1 Hz, 3H). 13C NMR (101 MHz, DMSO-d6) δ 164.68, 162.85, 157.40, 150.74, 143.10, 140.75, 133.80, 129.94, 127.16, 123.93, 122.97, 122.76, 121.00, 120.89, 114.50, 110.45, 109.45, 37.89, 14.21. ESI-MS [M+1] m/z 334.52.

2.2. Synthesis of 5-((9-ethyl-9H-carbazol-3-yl)methylene)-2-thioxodihydropyrimidine-4,6(1H,5H)-dione (EC-TBA)

Scheme S2

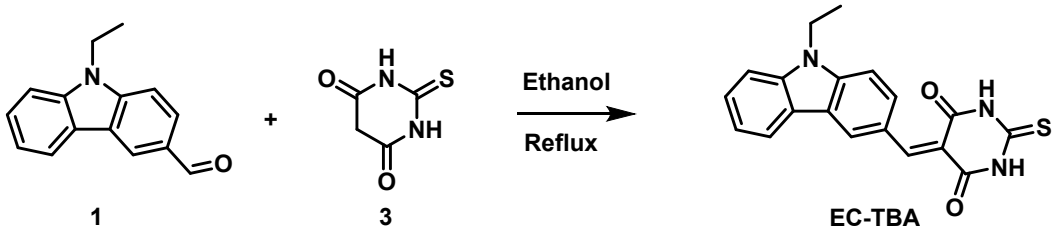

In a 100 mL round bottom flask, 9-ethyl-9H-carbazole-3- carbaldehyde (1) (0.5 g and 2.2 mmol) and thiobarbituric acid (3) (0.32 g and 2.2 mmol) was dissolved in 30 mL ethanol. The mixture was refluxed overnight with stirring at 85 °C during which an orange precipitate was formed. The precipitate was separated by filtration using Whatman filter paper 42 and washed thrice with 20 mL cold ethanol and the product was then dried using rotary evaporator which

offered an orange solid (0.51 g 91 %). 1H NMR (400 MHz, DMSO-d6) δ 12.38 (s, 1H), 12.29 (s, 1H), 9.33 (s, 1H), 8.66 (dd, J = 9.0, 1.7 Hz, 1H), 8.53 (s, 1H), 8.18 (d, J = 7.7 Hz, 1H), 7.71 (t, J = 8.9 Hz, 2H), 7.54 (ddd, J = 8.2, 7.1, 1.2 Hz, 1H), 7.33 (t, J = 7.5 Hz, 1H), 4.50 (q, J = 7.1 Hz, 2H), 1.35 (t, J = 7.1 Hz, 3H). 13C NMR (101 MHz, DMSO-d6) δ 178.60, 162.97, 160.61, 158.45, 143.55, 140.82, 134.2, 130.56, 127.33, 124.14, 123.00, 122.94, 121.14, 121.08, 114.51, 110.62, 109.67, 37.98, 14.24. ESI-MS [M+1] m/z 350.51.

Table S1 Absolute fluorescence quantum yields measured using an integrating sphere accessory

Ag: EC-TBA ratio	**Quantum Yield (%)**
1:0.5	1.58
1:1	1.98
1:2	1.83
1:3	1.64

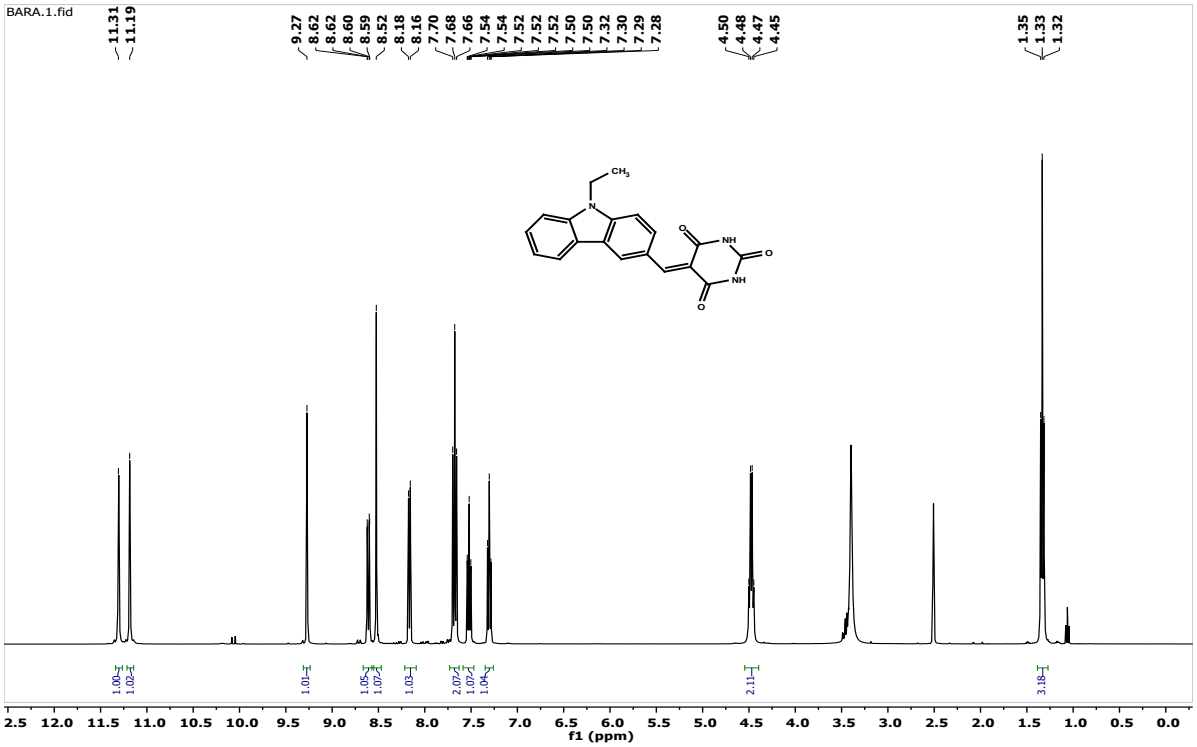

Fig. S1. ^{1}H NMR spectrum of **EC-BA** in DMSO-D6.

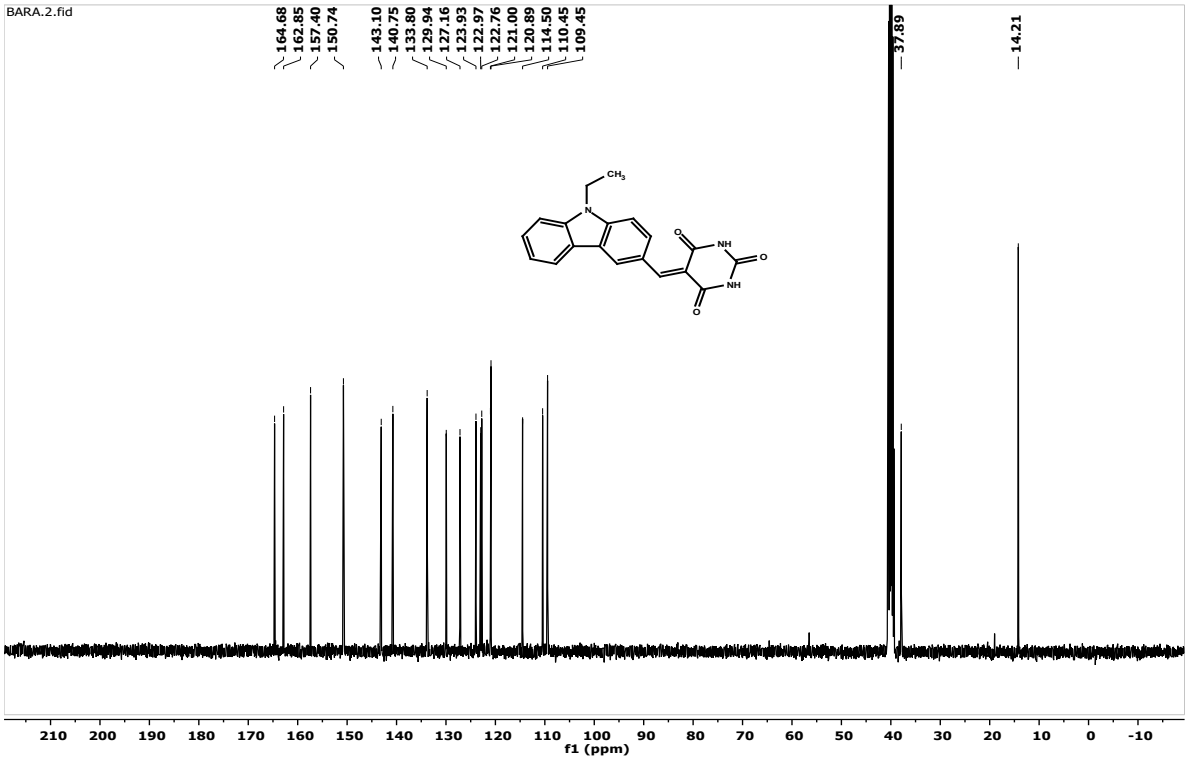

Fig. S2. ^{13}C NMR spectrum of **EC-BA** in DMSO-D6.

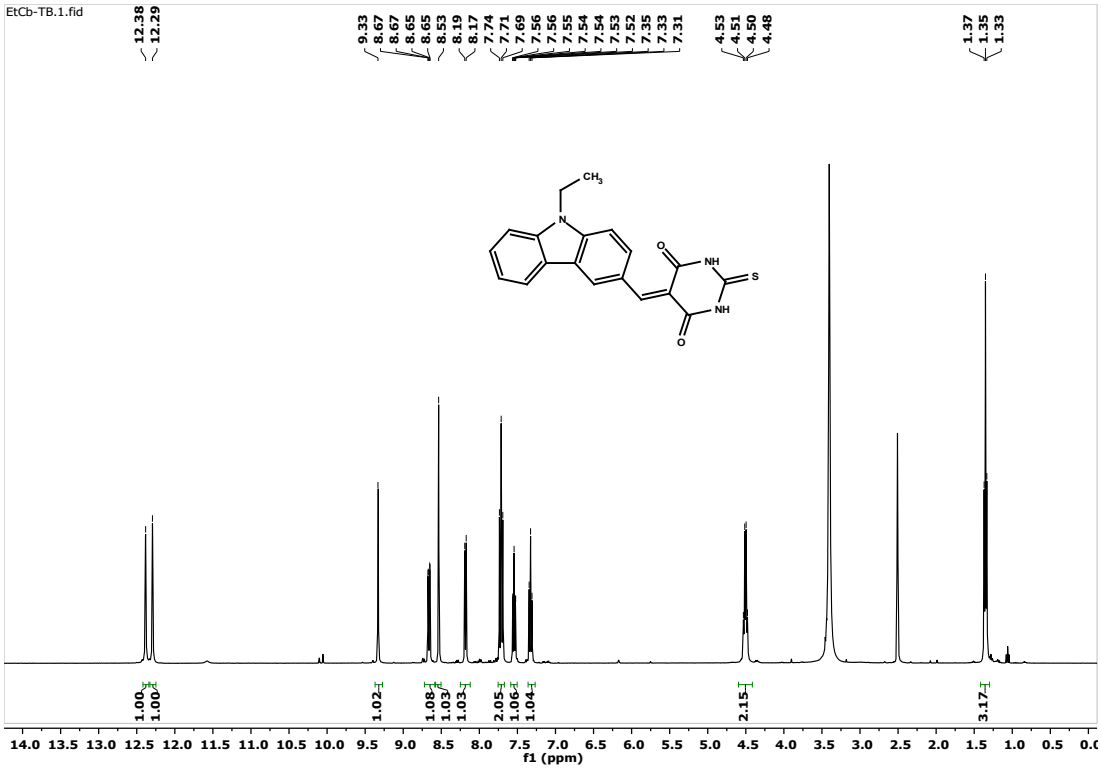

Fig. S3. [1]H NMR spectrum of **EC-TBA** in DMSO-D6.

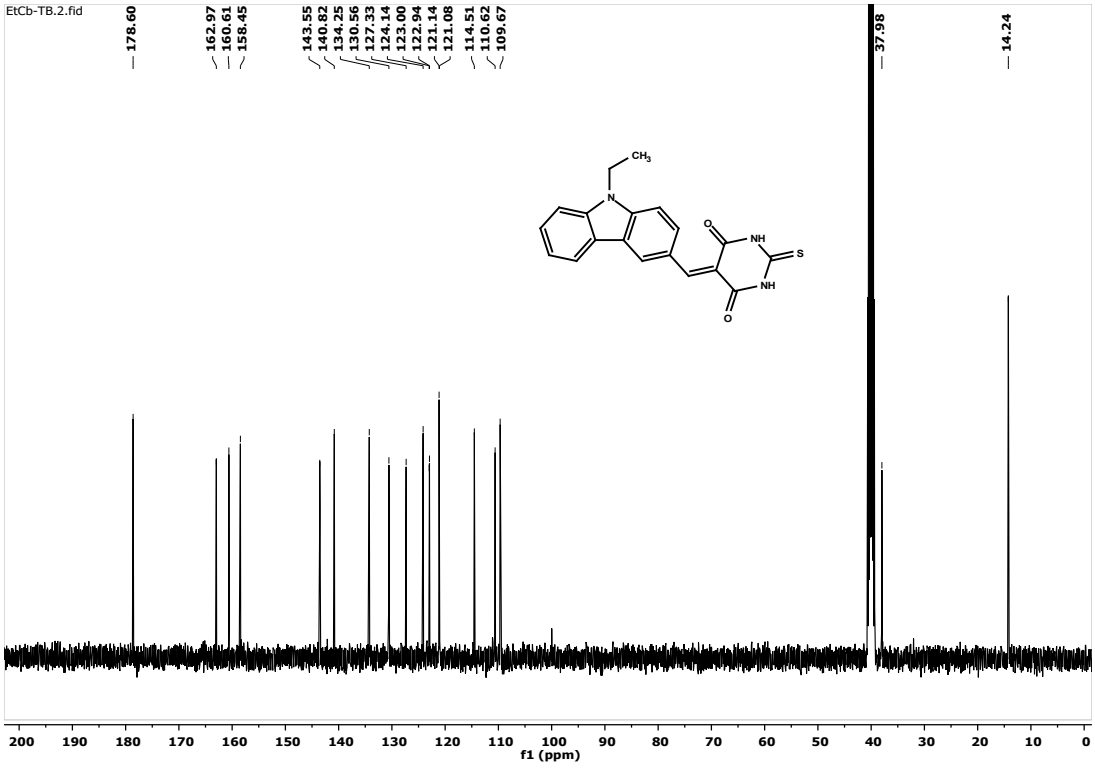

Fig. S4. [13]C NMR spectrum of **EC-TBA** in DMSO-D6.

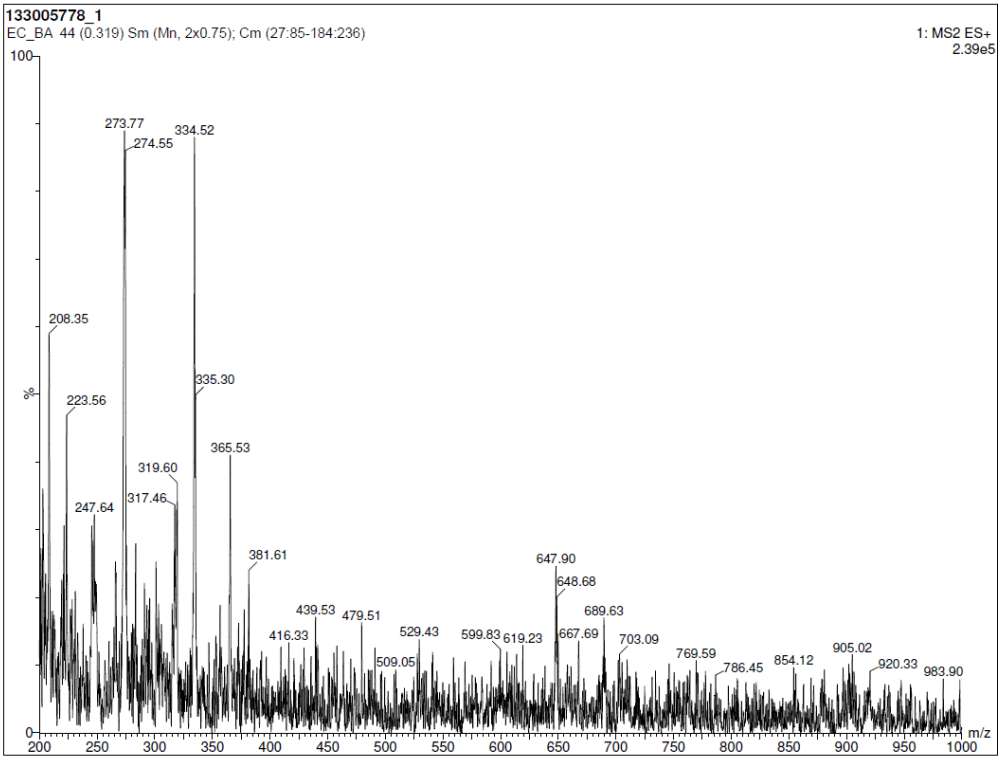

Fig. S5. ESI-MS spectrum of **EC-BA** in Methanol.

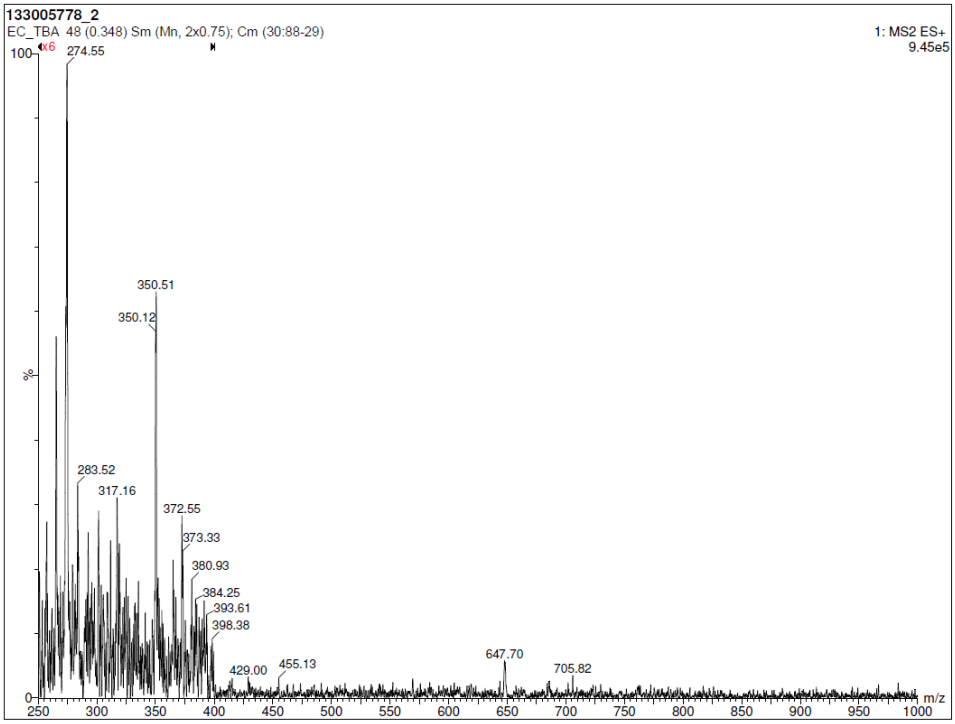

Fig. S6. ESI-MS spectrum of **EC-TBA** in Methanol.

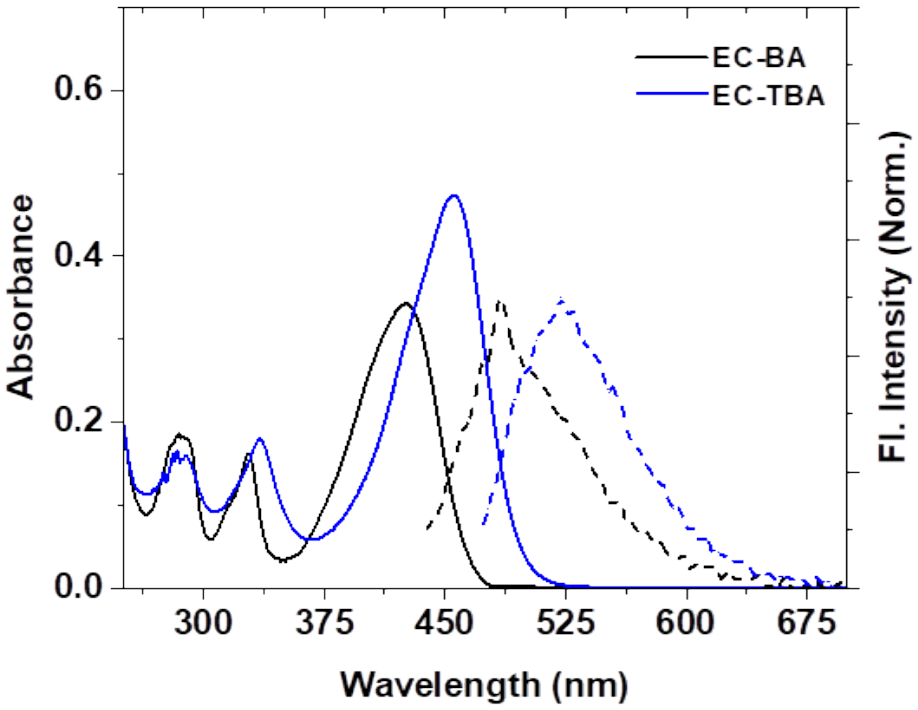

Fig. S7. UV-visible absorption (solid line) and fluorescence (dotted line) spectra of **EC-BA** and **EC-TBA** in THF solution.

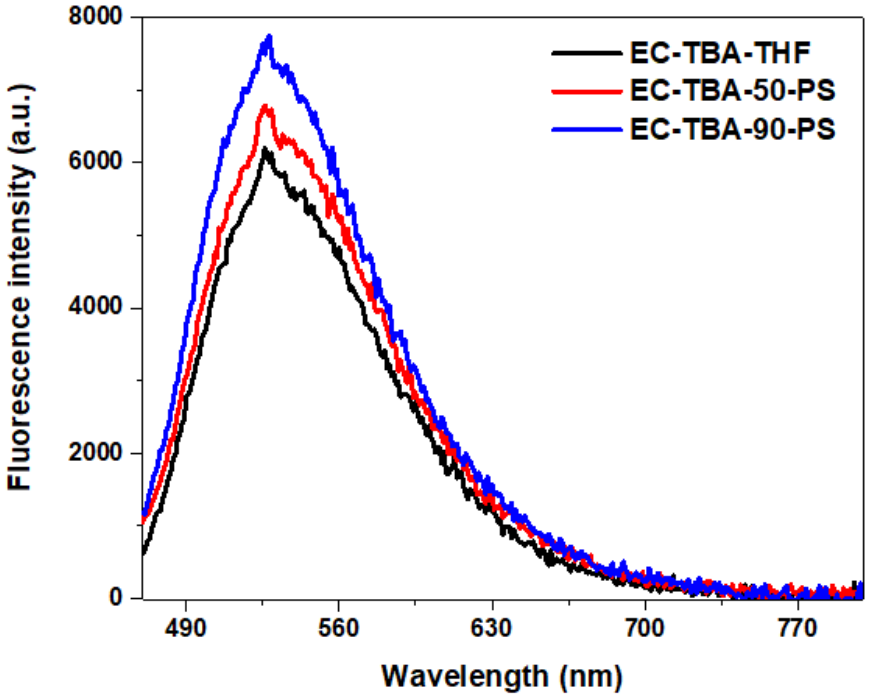

Fig. S8. Emission spectrum of EC-TBA in THF with the 5% and 10% of the saturated polystyrene solution in THF (vol/vol).

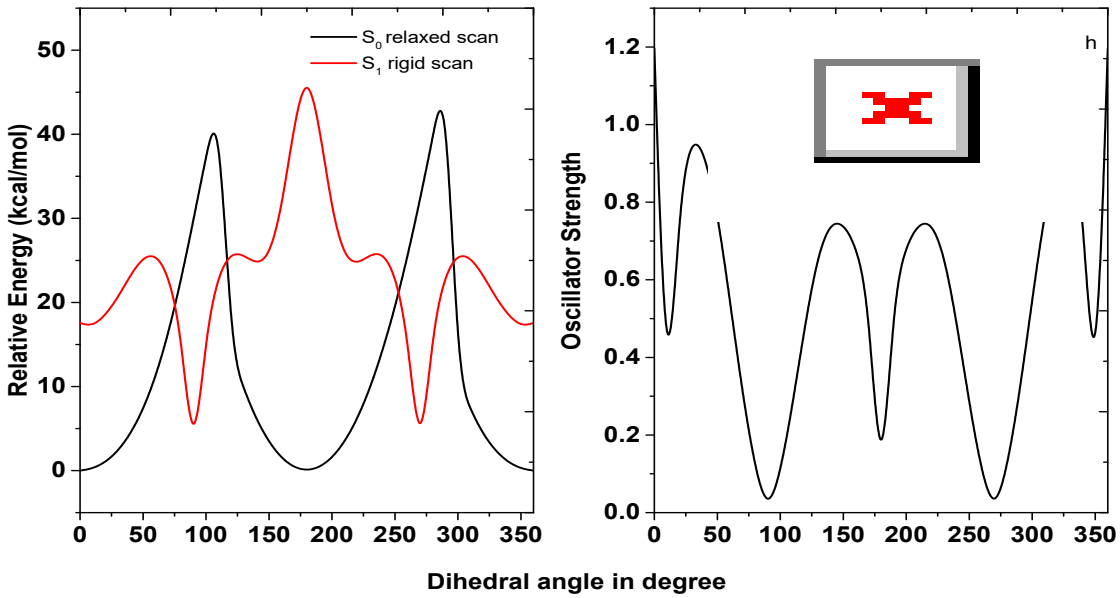

Fig. S9. Plot of dihedral angle versus the relative energy (left panel) and oscillator strength (right panel).

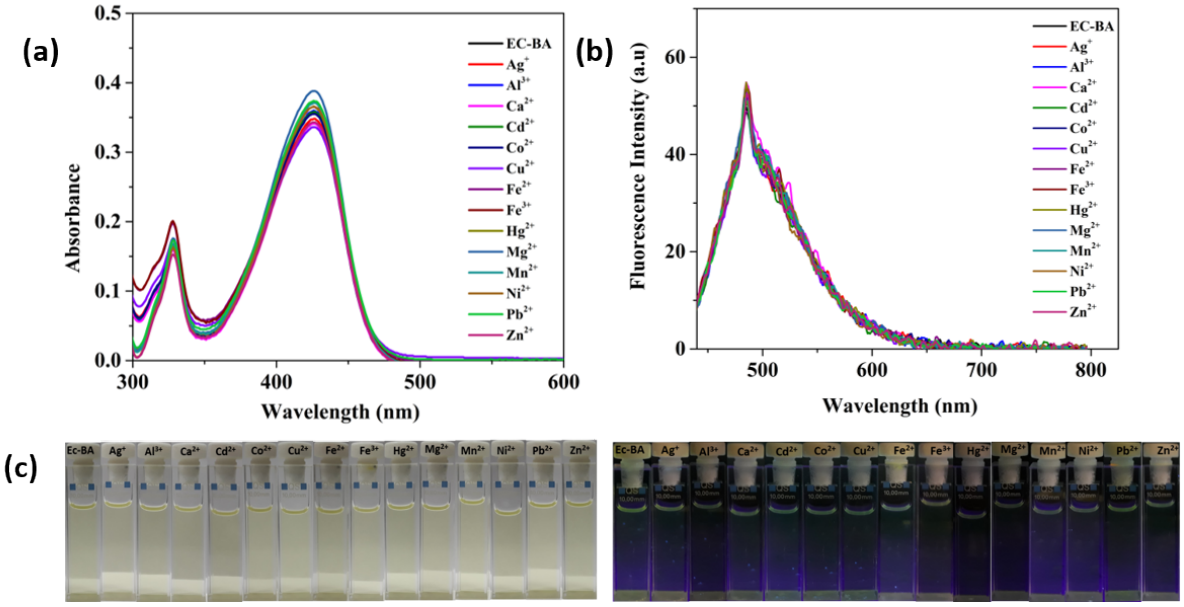

Fig. S10. a) UV-visible absorption spectrum, b) emission spectrum of **EC-BA** (10 μM) in 1:2 complexes with Ag^{+}, Al^{3+}, Ca^{2+}, Cd^{2+}, Co^{2+}, Cu^{2+}, Fe^{2+}, Fe^{3+}, Hg^{2+}, Mg^{2+}, Mn^{2+}, Ni^{2+}, Pb^{2+} and Zn^{2+} in THF/water medium, c and d are the digital images of the solution respectively under ambient light and UV excitation.

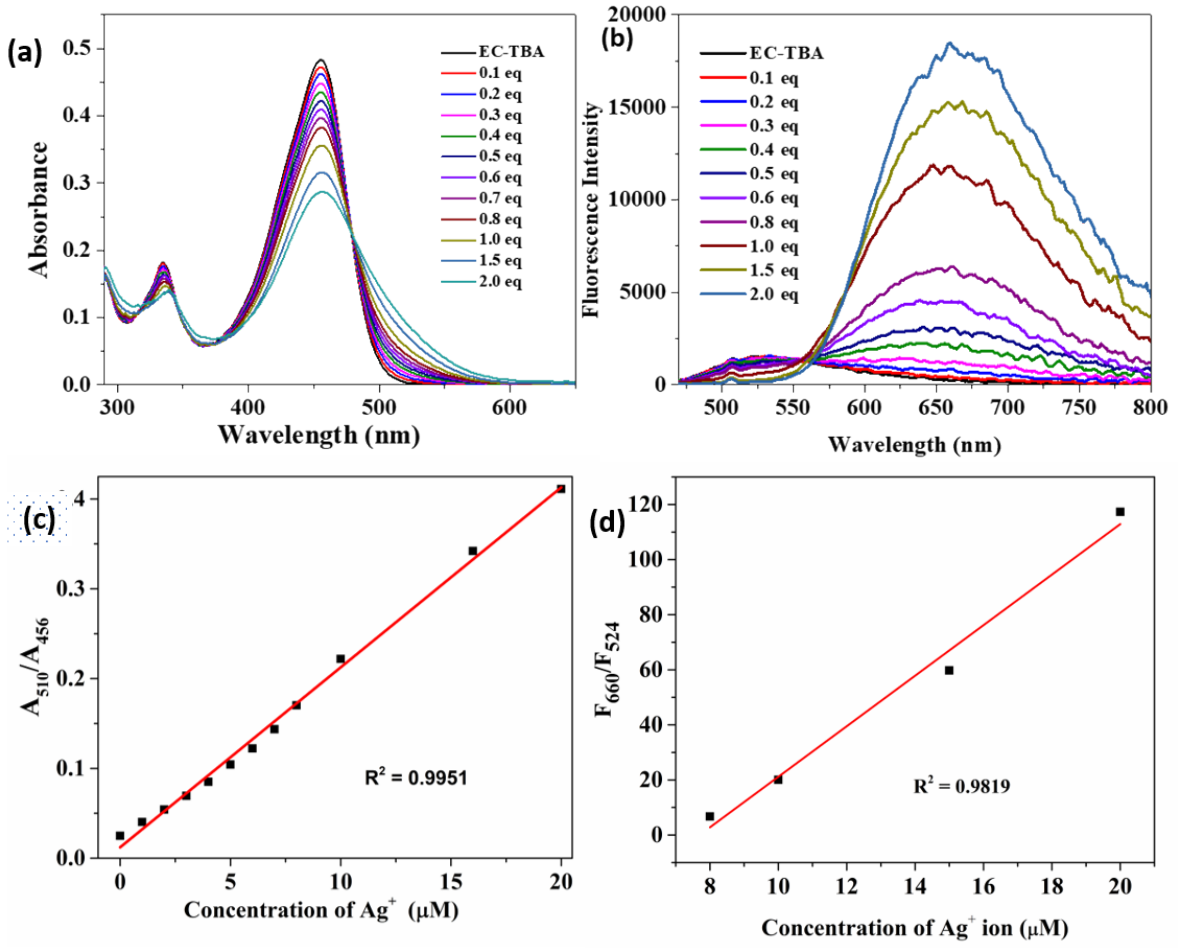

Fig. S11. (a) Absorption (b) Fluorescence ratiometric titration spectrum of **EC-TBA** (10 μM) with Ag^+ (c) Plot of [Ag^+] vs ratiometric absorption (d) Plot of [Ag^+] vs ratiometric fluorescence intensity at different concentrations of Ag^+ ions.

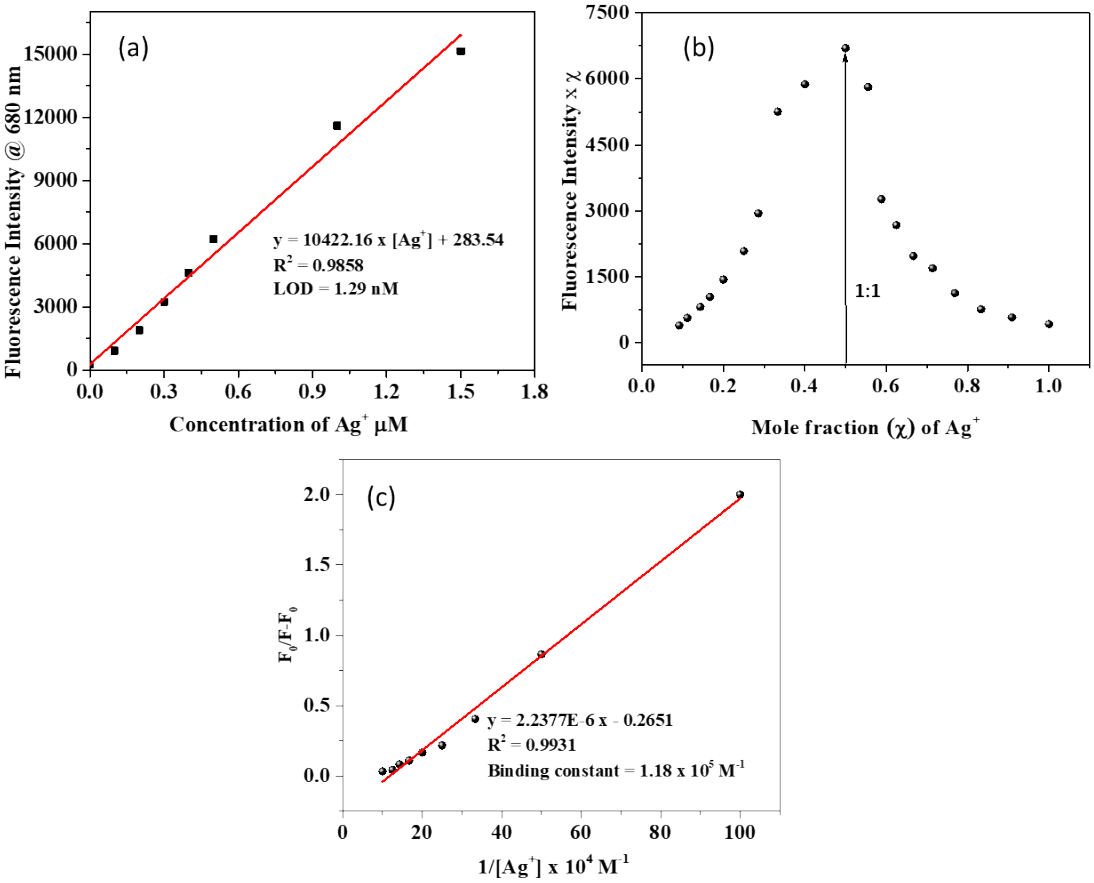

Fig. S12. (a) Fluorescent intensity at 680 nm vs Ag^+ ion concentration (b) Job's plots and (c) Benesi-Hildebrand plot.

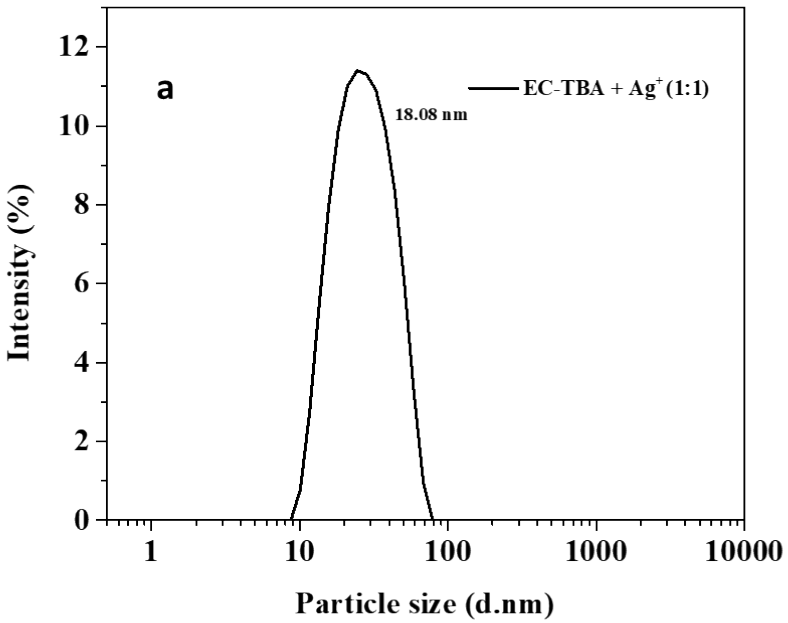

Results

		Mean (mV)	Area (%)	St Dev (mV)
Zeta Potential (mV): -26.2	Peak 1:	-26.2	100.0	6.03
Zeta Deviation (mV): 6.03	Peak 2:	0.00	0.0	0.00
Conductivity (mS/cm): 0.0164	Peak 3:	0.00	0.0	0.00
Result quality : Good				

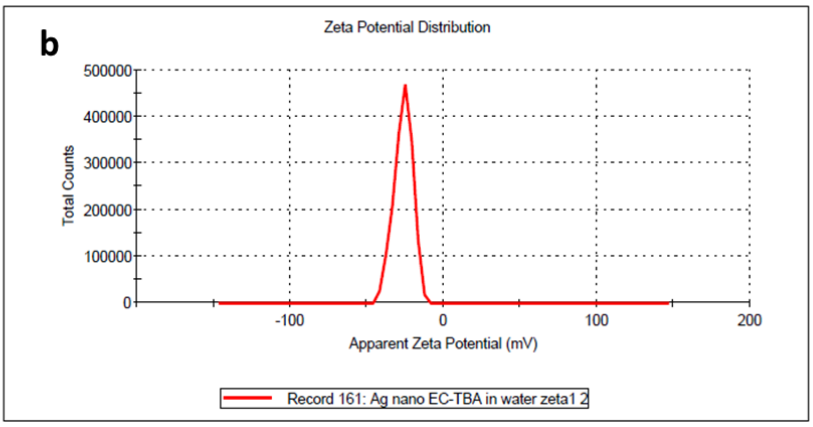

Fig. S13. (a) Particle size distribution from DLS measurements (b) Zeta potential of Ag nanocluster in THF/Water.

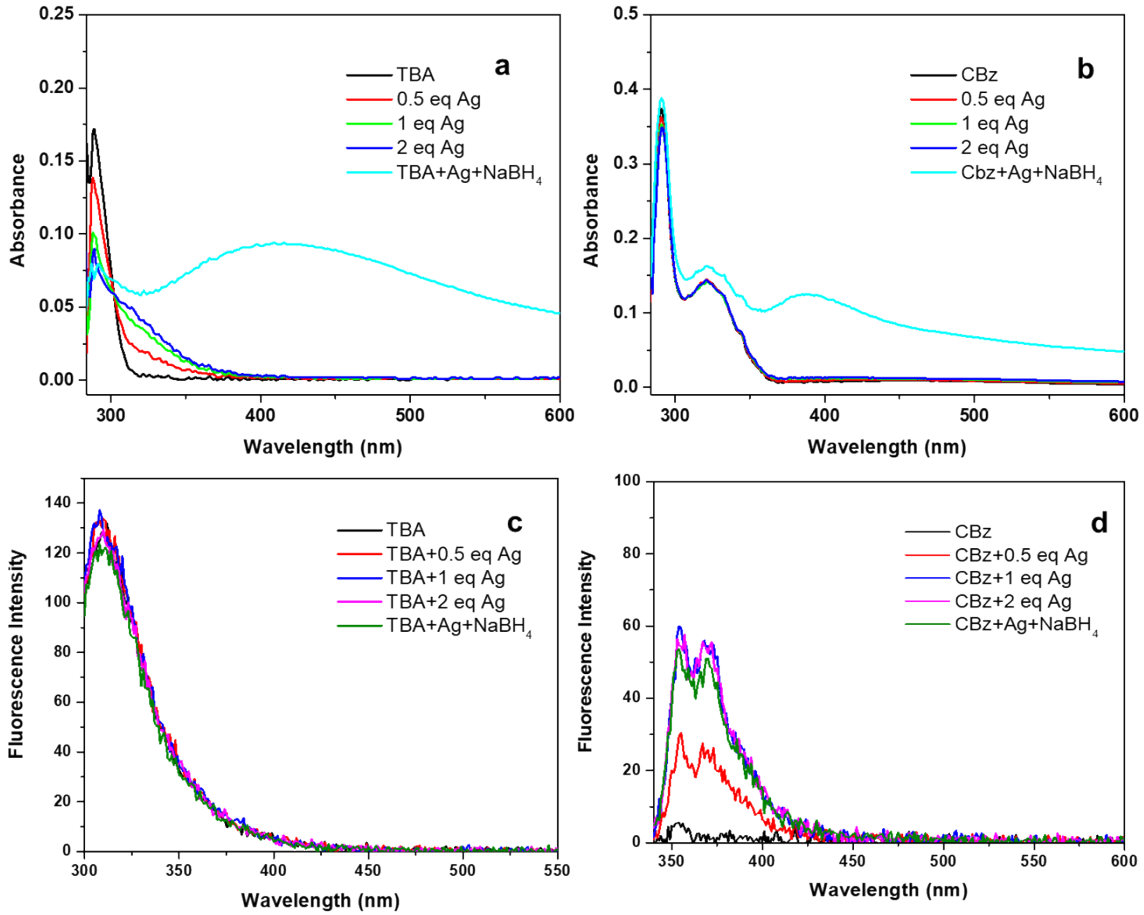

Fig. S14. UV-visible absorption spectra of a) TBA and b) Carbazole in THF in the presence of different equivalents of silver ion and silver ion + $NaBH_4$. Corresponding fluorescence spectra of c) TBA and d) Carbazole under similar experimental conditions.

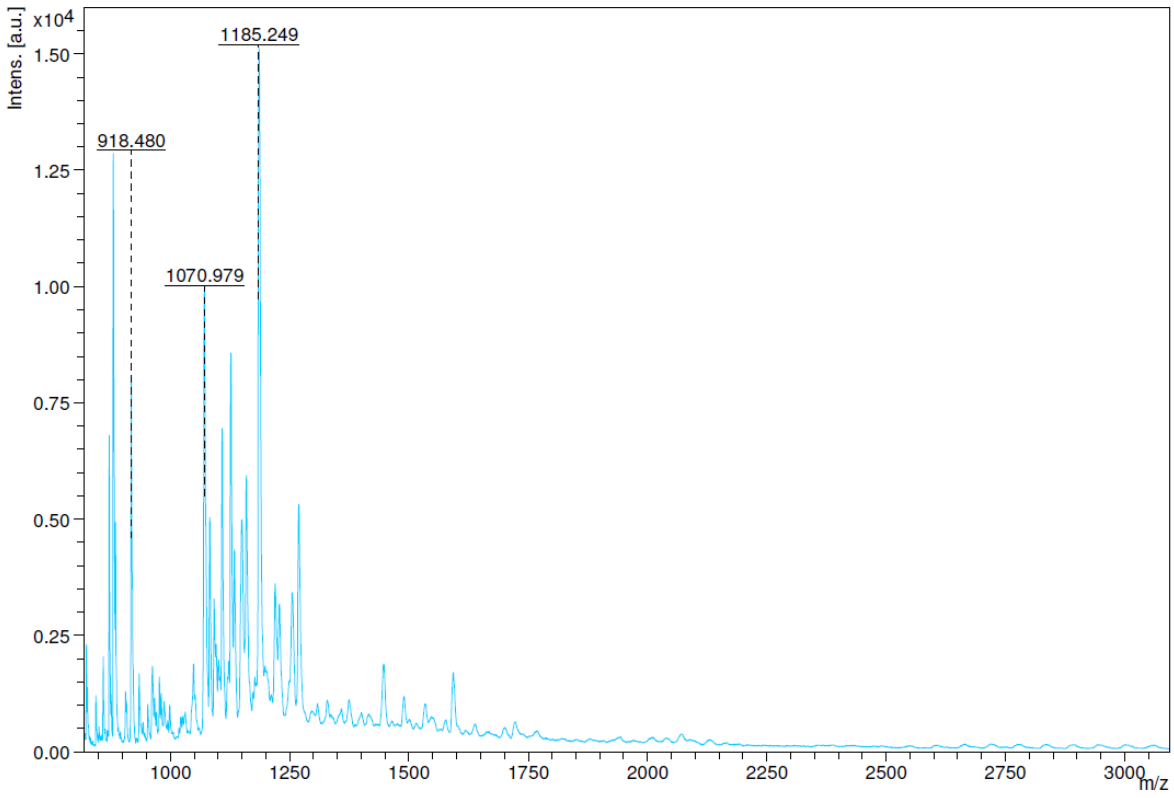

Fig. S15. MALDI TOF MS of silver nanoclusters.

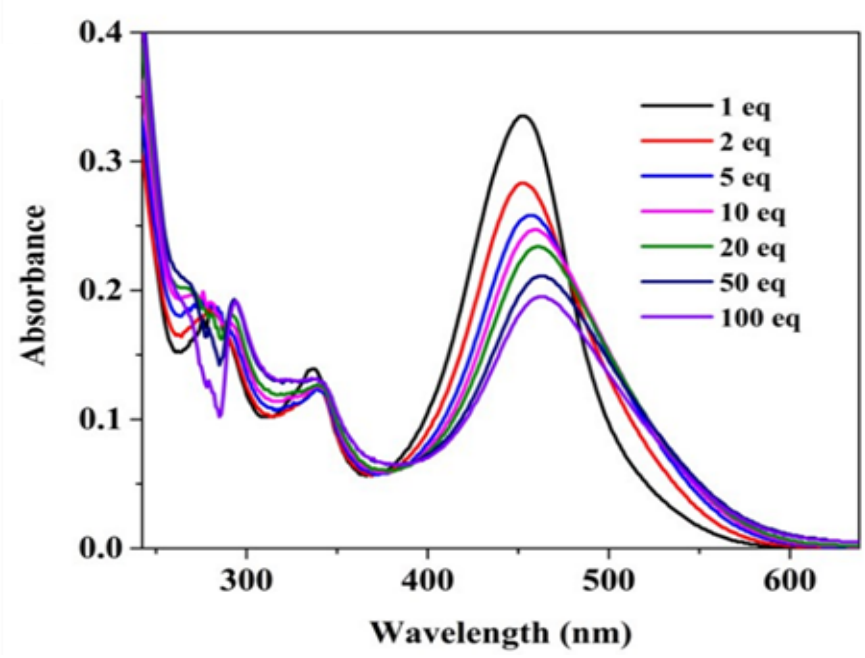

Fig. S16. UV-visible absorption spectra of **EC-TBA** in THF in the presence of different molar equivalents of silver ions.

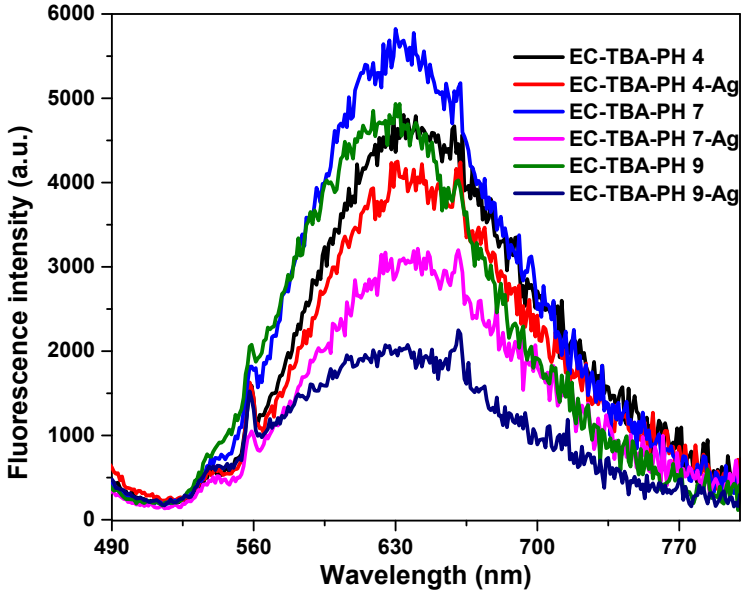

Fig. S17. pH-dependent emission spectra of the Ag nanocluster.

References

1. Frisch, M. J.; Trucks, G. W.; Schlegel, H. B.; Scuseria, G. E.; Robb, M. A.; Cheeseman, J. R.; Scalmani, G.; Barone, V.; Petersson, G. A.; Nakatsuji, H.; Li, X.; Caricato, M.; Marenich, A. V.; Bloino, J.; Janesko, B. G.; Gomperts, R.; Mennucci, B.; Hratchian, H. P.; Ortiz, J. V.; Izmaylov, A. F.; Sonnenberg, J. L.; Williams; Ding, F.; Lipparini, F.; Egidi, F.; Goings, J.; Peng, B.; Petrone, A.; Henderson, T.; Ranasinghe, D.; Zakrzewski, V. G.; Gao, J.; Rega, N.; Zheng, G.; Liang, W.; Hada, M.; Ehara, M.; Toyota, K.; Fukuda, R.; Hasegawa, J.; Ishida, M.; Nakajima, T.; Honda, Y.; Kitao, O.; Nakai, H.; Vreven, T.; Throssell, K.; Montgomery Jr., J. A.; Peralta, J. E.; Ogliaro, F.; Bearpark, M. J.; Heyd, J. J.; Brothers, E. N.; Kudin, K. N.; Staroverov, V. N.; Keith, T. A.; Kobayashi, R.; Normand, J.; Raghavachari, K.; Rendell, A. P.; Burant, J. C.; Iyengar, S. S.; Tomasi, J.; Cossi, M.; Millam, J. M.; Klene, M.; Adamo, C.; Cammi, R.; Ochterski, J. W.; Martin, R. L.; Morokuma, K.; Farkas, O.; Foresman, J. B.; Fox, D. J. *Gaussian 16 Rev. A.03*, Wallingford, CT, 2016.
2. Yanai, T.; Tew, D. P.; Handy, N. C., A new hybrid exchange–correlation functional using the Coulomb-attenuating method (CAM-B3LYP). *Chemical Physics Letters* **2004,** *393* (1), 51-57.
3. Grimme, S.; Antony, J.; Ehrlich, S.; Krieg, H., A consistent and accurate ab initio parametrization of density functional dispersion correction (DFT-D) for the 94 elements H-Pu. *The Journal of Chemical Physics* **2010,** *132* (15).

4. Petersson, G. A.; Al-Laham, M. A., A complete basis set model chemistry. II. Open-shell systems and the total energies of the first-row atoms. *The Journal of Chemical Physics* **1991,** *94* (9), 6081-6090.